Marine Geology 446 (2022) 106770

Contents lists available at ScienceDirect

Marine Geology

journal homepage: www.elsevier.com/locate/margo

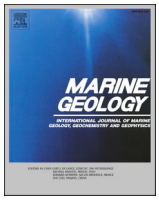

Research Article

Complex drivers of reef-fronted beach change

Anna B. Mikkelsen *, Tiffany R. Anderson, Sloan Coats, Charles H. Fletcher

Department of Earth Sciences, School of Ocean and Earth Science and Technology, University of Hawai'i at Mānoa, Honolulu, HI 96822, USA

ARTICLE INFO

Keywords:
Carbonate beach
Coastal processes
UAS surveys
Environmental monitoring
Hawai'i
Self-organizing maps

ABSTRACT

Royal Hawaiian Beach in Waikīkī plays an essential role in Hawai'i's tourism-based economy. To inform development of management policies, we conduct two years of weekly ground and aerial surveys (April 2018 to February 2020) to track change on this chronically eroding beach. We use multiple linear regressions, Self-Organizing Maps (a form of cluster analysis), remotely sensed nearshore sand fields, hydrodynamic modelling, and monitoring of key physical processes to identify the principal drivers of beach change. Our results show 12 months of subaerial accretion ($+2400 \pm 59$ m^3) followed by 10 months of erosion (-3090 ± 51 m^3) for a net loss of 690 ± 51 m^3, and document that interannual variations in beach width and volume overprint seasonal patterns. Notably, a seasonal signal is recorded in the topographic structure of the beach. We test the relationship of beach volume and width to variations in wind, water level, wave energy flux generated from southern hemisphere swell, and wave energy flux from locally generated trade-wind waves. We identify three beach segments and three nearshore sand fields that form a sand-sharing, source-sink network, yet operate quasi-independently. Our analysis reveals that individual beach segments and their adjacent sand fields experience coherent (simultaneous) gains and losses of sand, suggesting that alongshore sediment exchange is dominant over cross-shore exchange. The main drivers of beach change are variations in water level and wave energy flux. Beach volume and width both vary with nearshore sand cover, indicating that free exchange with nearshore sources is intrinsic to beach variability. Our results suggest that rising sea level and extreme El Niño-Southern Oscillation events will contribute to Royal Hawaiian Beach destabilization, which may amplify erosional events and increase the cost of future beach maintenance.

1. Introduction

Reef-fronted beaches are important assets providing ecological services (Barbier et al., 2011), storm buffers (El Mrini et al., 2012), critical habitat for coastal flora and fauna, economic development (Houston, 2008), and recreational opportunities for residents and visitors. As beach systems face anthropogenic stressors such as encroaching development and sea level rise (SLR), it is critical that managers have a detailed understanding of environmental processes driving beach change. Yet, carbonate beaches are complex systems that remain poorly understood (Jeanson et al., 2013; Risandi et al., 2020; Segura et al., 2018). Intricate reef bathymetry results in cryptic interactions among natural and anthropogenic forces making it difficult to isolate cause and effect relationships. Nonetheless, to underpin effective management in a future characterized by SLR (Oppenheimer et al., 2019) and amplified storm impacts (Knutson et al., 2020) it is critical to continue improving our understanding of how and why beaches change.

Environmental controls on beach morphology for open coasts and reef-fronted beaches are governed by variability in waves, wind, water level, currents, and processes on geologic timescales. Wave processes control sediment transport from (1) wave breaking and resulting radiation stress gradients driving nearshore currents (Gourlay and Colleter, 2005; Monismith et al., 2013), and (2) long period, low amplitude infragravity waves (typically non-breaking), that produce both wave setup (Buckley et al., 2018; Pomeroy et al., 2012), and standing waves that drive cross-shore and alongshore currents (Özkan-Haller et al., 2001; Winter et al., 2017). For open coasts, these wave mechanisms are the primary forces driving rotation between reflective (accreted) and dissipative (eroded) beach states (Wright and Short, 1984). In addition to wave climate, water level controls beach systems on timescales from decadal (change of shoreline position) to interannual and tidal variations in beach morphology. Prolonged elevated water levels have been associated with erosion on magnitudes similar to erosion during large storms (Abessolo et al., 2020; Theuerkauf et al., 2014), while extreme

* Corresponding author.
E-mail address: abm20@hawaii.edu (A.B. Mikkelsen).

https://doi.org/10.1016/j.margeo.2022.106770
Received 11 December 2021; Received in revised form 5 March 2022; Accepted 8 March 2022
Available online 15 March 2022

tidal events (e.g., king tides) are associated with beach narrowing and erosion (Banno and Kuriyama, 2020; Clarke et al., 1984; Roman-Rivera and Ellis, 2018). Climate patterns such as the El Niño Southern Oscillation (ENSO) and Pacific Decadal Oscillation (PDO) that are responsible for basin scale changes in wave energy, wave direction, and water level, have also been connected to changes in beach erosion patterns (Barnard et al., 2015; Vos et al., 2021).

Reef-fronted beaches are governed by these same processes, but intricate reef bathymetry produces variations in bottom roughness and slope that add complexity to nearshore hydrodynamics and complicate beach responses to environmental conditions. Higher water levels can increase wave energy transmission across the reef (Ferrario et al., 2014; Péquignet et al., 2011), and increase sediment transport (Grady et al., 2013). Past studies of reef-fronted beaches have shown that small increases in water level can lead to beach erosion (Anderson et al., 2015; Segura et al., 2018) or accretion if nearshore currents favor sediment deposition (Baldock et al., 2015; Risandi et al., 2020). Typically, seasonal patterns are evident in shoreline position, beach volume, or alongshore beach rotation (Dail et al., 2000; Jeanson et al., 2013; Norcross et al., 2002; Segura et al., 2018)

Reef-fronted beaches are globally distributed. Despite this, our knowledge of the primary forces that drive change at reef-fronted beaches remains poor. Monitoring environmental conditions and relating them to unique sediment connections between the subaerial beach and nearshore, is critical to an improved understanding of beach system dynamics. This will require high spatial and temporal monitoring of both the subaerial beach and nearshore and, as such, here we compare weekly observations of beach and sand field characteristics with local environmental conditions.

Small unoccupied aerial systems (sUAS) allow for data collection of high spatial and temporal resolution and have become a fundamental tool in monitoring earth surface processes (Eltner et al., 2016; Fonstad et al., 2013) including coastal environments (Casella et al., 2016; Gonçalves and Henriques, 2015; Turner et al., 2016). Coastal studies using sUAS have focused on seasonal changes (Laporte-Fauret et al., 2019; Scarelli et al., 2017), post-storm monitoring (Turner et al., 2016), coastal habitats (Nolet et al., 2018; Varela et al., 2019), and interannual changes (Pagán et al., 2019).

While sUAS has become an essential tool for monitoring coastlines, it remains limited in resolving foreshore and nearshore sediments in beach systems. Run-up in the swash zone, saturated sand, sun glint, turbid water, and whitewater create high motion areas that do not render well when performing structure-from-motion on sUAS images. In traditional coastal topographic surveys, beach profiles provide a coarse record of nearshore variability (Habel et al., 2016; Norcross et al., 2002), and classic shoreline change models include proxies for nearshore sediment exchange (Bruun, 1962; Wright and Short, 1984). Surveying solely the subaerial beach neglects this essential part of beach systems.

Most nearshore sand deposits on reef-fronted beaches are thin and redistribute quickly in response to wave stress, consequently covering or uncovering rocky (fossil reef) benthic substrate (Conger et al., 2009). Clear water and shallow conditions permit these shifts in sand cover to be captured in sUAS imagery. We develop a binary benthic classification (rock/sand) to observe sand covering/uncovering of rocky substrate and infer changes in nearshore sand fields. The classification is coupled with sUAS photogrammetry of the subaerial beach to produce a dataset that includes both subaerial and nearshore sediments to explore complex sediment movement at a reef-fronted beach.

Using two years of weekly sUAS observations, we monitor changes in beach characteristics and compare this history with physical drivers of beach change including wave, wind, and water level records using multiple linear regressions. We correlate these changes with three nearshore sand fields and investigate variations in beach topography using an artificial neural network clustering method known as Self-Organizing Maps (SOMs). The objectives of this study are to record a history of beach characteristics and nearshore sand fields and answer the following: (1) What are the primary environmental variables that drive beach change? (2) Is there a seasonal structure to beach volume and width, and topography? (3) How are adjacent nearshore sand fields connected to the subaerial beach – that is, is sediment exchange dominated by cross-shore or alongshore sediment movement, and what processes drive sediment exchange between the nearshore sand fields and subaerial beach?

2. Regional setting

Royal Hawaiian Beach in Waikīkī (Fig. 1) plays an essential role in Hawai'i's tourism-based economy that is valued at ~$2.2 billion annually (Tarui et al., 2018). Previous studies have established that the beach is characterized by chronic erosion punctuated by seasonal variation (Miller and Fletcher, 2003), and that seasonal morphologic change (Habel et al., 2016) corresponds to summer accretion promoted by south swell, and erosion promoted by local trade-wind swell (intermittent year-round). However, past studies have relied on relatively coarse temporal (quarterly to interannual) and spatial (multimeter) resolution. Considering the critical economic role of Royal Hawaiian Beach, and the rapid growth of anthropogenic stressors such as SLR, coastal development, increased storm intensity, and reef degradation (Hoegh-Guldberg et al., 2007; IPCC, 2021; Knutson et al., 2020; Oppenheimer et al., 2019), optimized beach management policies need high temporal and spatial resolution monitoring and analysis.

The Hawaiian coastline is dominated by variable oceanographic conditions, principally seasonal swell and locally-generated waves. The wave field comprises four dominant regimes (Fletcher et al., 2008; Vitousek and Fletcher, 2008). (1) Winter swells with periods of 14–20 s and breaking face heights of 2–15 m are generated by storms in the North Pacific. These north swells are blocked by the island and have little influence on Waikīkī beaches. (2) Summer swells generated by storms in the Southern Ocean with periods of 14–22 s and heights of 1–5 m are prominent from April to October. (3) Locally-generated trade-wind waves, the most common wave type in Hawai'i, are short period (6–10 s) relatively low height (1–3 m) waves that persist year-round but are most frequent in the summer. (4) Originating from the south or south-west generally in the winter, Kona waves have relatively short periods of 8–10 s with heights of 3–5 m (Homer, 1964). Tropical cyclone swells occasionally impact Hawai'i's shores from June to November bringing greater wave energy that enhances run-up and can drive significant beach erosion and sediment redistribution (Fletcher et al., 2003).

Ocean water level variability is driven by seasonal heating, tidal effects, and interannual climate patterns (Devlin et al., 2017; Potemra and Lukas, 1999; Widlansky et al., 2020). Monthly average water levels vary by 0.1 m (typically lowest in March and highest in September). The maximum spring tide range is about 1 m, with highest water levels occurring during the summer spring perigee. Other drivers of water level variability (10's of cm) include mesoscale eddies (Firing and Merrifield, 2004), and interannual thermal and wind field influences (Long et al., 2020). The Honolulu tide station (NOAA, 2020), records a long term SLR of 1.55 ± 0.21 mm/year (1905–2020) that, since the year 2000, has increased to 3.5 ± 0.12 mm/year (data accessed July 2020; Caldwell et al., 2015).

To date, the primary management response to erosion on Royal Hawaiian Beach has been periodic sand nourishment (Wiegel, 2008; Habel et al., 2016) utilizing adjacent shallow reef top sand fields as borrow sites. Typical of other Hawaiian coastal segments (Bochicchio et al., 2009; Conger et al., 2009), nearshore sands in Waikīkī consist of carbonate skeletal fragments produced by the fringing reef ecosystem (Harney and Fletcher, 2003). The beach is fronted by a gently sloping fringing coral reef a few thousand feet wide (Wiegel, 2008). In the immediate nearshore, a sand field with intermittent rocky substrate (fossilized reef) extends seaward from the toe of Royal Hawaiian Beach approximately 100–200 m and shows changes in sand-rock distribution

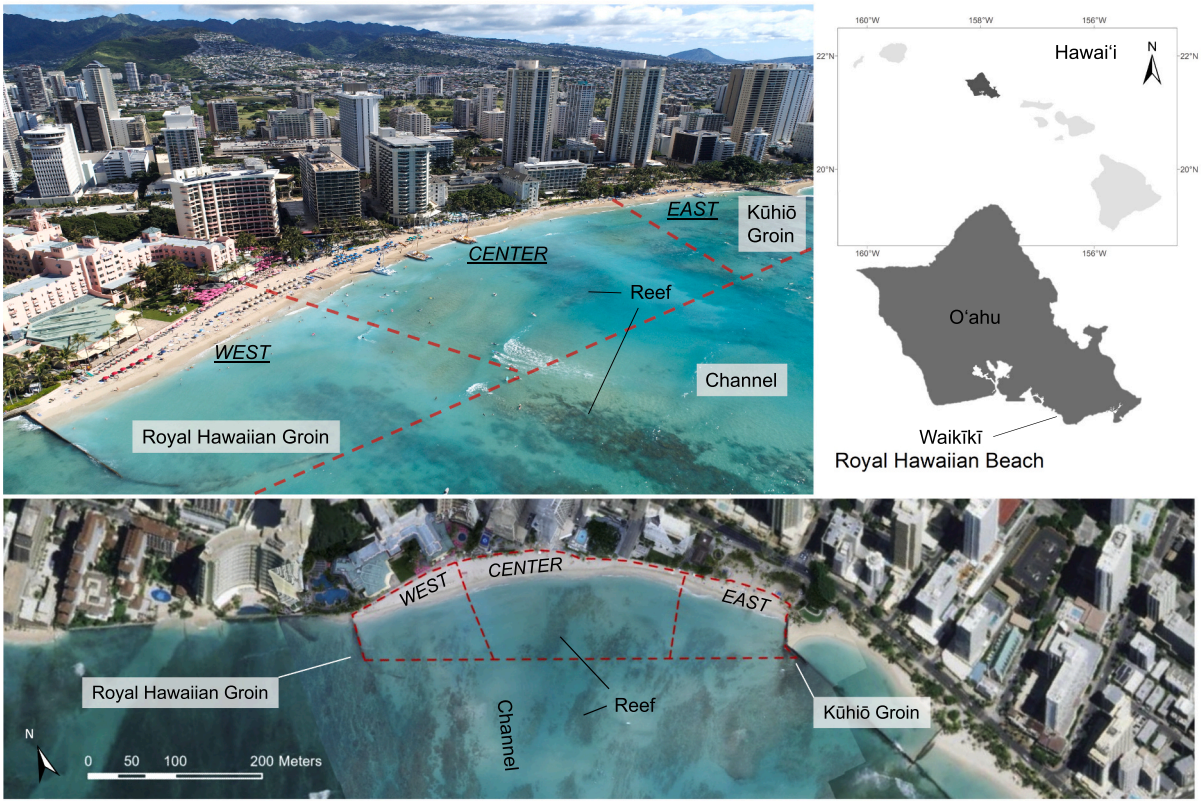

Fig. 1. Royal Hawaiian Beach, located in Waikīkī on the south shore of O'ahu, extends 500 m between Kūhiō Groin to the east and Royal Hawaiian Groin to the west. These terminal groins create a littoral cell that is largely closed to external alongshore sand exchange. Also shown are three beach segments used in our analysis (east, center, west), and three adjacent offshore sand fields. A shallow fringing reef platform influences wave characteristics incident to the east and west portions of the beach (dark benthic substrate). Adjacent to the central portion of the beach a break in the fringing reef forms a shallow, low-relief, sand-filled channel.

that vary with beach morphology. It is a popular beach that is heavily trafficked for recreation, leisure, and exercise, but there is no seasonal beach reprofiling or mechanical cleaning except during occasional nourishment projects.

3. Methods

3.1. Field data

Seventy-two weekly aerial and ground surveys were collected between April 2018 and February 2020, with a nine-week gap from November 2018 to January 2019. Surveys were scheduled randomly with respect to tide and wave conditions. An sUAS (DJI Phantom 4 pro) collected images at 120 m altitude with 80% front and side overlap, producing orthomosaics with a resolution of 3 to 3.5 cm/pixel. Seven ground control points (GCPs) were spaced about 100 m alongshore. Additional control points, collected every 5–10 m using a rod-mounted prism and a Leica TS16 Robotic Total Station, defined the position of the low water mark (LWM) at the seaward edge of the foreshore (Norcross et al., 2002; Fletcher et al., 2003). Existing benchmarks provided a spatial reference using the WGS 1984 UTM Zone 4 projection. Elevations were measured with respect to local mean sea level (LMSL; Datums – NOAA Tides and Currents, present epoch: 1983–2001).

Using Agisoft Metashape and LAStools, a dense point cloud and orthomosaic were generated from sUAS images following standardized USGS protocol (USGS, 2017a, 2017b). The low water mark (LWM) vector was merged with the sUAS point cloud, and a digital elevation model (DEM) was produced using a natural neighbor interpolation (0.5 m cell size) and smoothed using a 5 m circular mean filter (in ArcMap 10.7). Using the ArcMap (ESRI) *volume* tool, subaerial beach volume was calculated for each survey, with mean higher high water (MHHW: 0.329 m above MSL) serving as the lower elevation bound. As a result, the seaward boundary was delineated as the location where the beach face intersected the MHHW elevation contour, and the landward boundary was delineated by fixed backshore locations consisting of walls, paths, or other man-made structures. Beach width, the distance between a fixed backshore and the LWM (Norcross et al., 2002), was measured using ArcMap (ESRI) at 100 digital cross-shore transects spaced 5 m alongshore. To assess width in three beach segments of interest, digital transects within each segment were averaged for each survey. To assess comparable changes in volume and width, the timeseries was normalized (0 to 1) using a standard normalizing equation $(x - x_{min}) / (x_{max} - x_{min})$, where x represents the volume or width of that beach segment.

To quantify uncertainty for volume measurements, an independent survey was conducted, in which measured point elevations (collected with the Leica TS16 Robotic Total Station, $n = 198$) were compared to modelled point elevations extracted from an sUAS-derived DEM. We calculate the variance, or standard error, between modelled and measured points (SE = 0.005 m) for use as vertical uncertainty, as we find no bias and assume errors are randomly distributed ($\mu = 0.004\ m$; $\sigma = 0.068\ m$). Volume uncertainty is the footprint beach area times the SE. Beach width uncertainty (±0.3 m cross-shore) is attributed to LWM measurement error determined by repeat surveys.

3.2. Nearshore sand cover

With a simple binary classification (sand vs rock) applied to the shallow marine portion of sUAS imagery, we identify weekly changes in nearshore sand cover. Where correlated to beach volume or width, we interpret this as a proxy for sand exchange between the beach and

shallow nearshore (Norcross et al., 2002). Imagery processing to identify changes in nearshore sand cover required cropping orthomosaics to a fixed area (Fig. 2A). Adjacent to the beach center, the cropped boundary is located approximately 95 m offshore of the beach LWM. Because of weekly variations in turbidity, automated binary classification proved unsuccessful. Instead, we apply an unsupervised classification (ISODATA; Iterative Self-Organizing Data Analysis Technique, ENVI 5.4) to group similar pixels into 10 classes (Fig. 2B) (Conger et al., 2005; Isoun et al., 2003). Only green (532 nm) and blue (468 nm) bands (Burggraaff et al., 2019) were used for classification as the red band introduced noise due to strong attenuation and resulted in misclassification. Due to high variability in light attenuation characteristics resulting from depth, turbidity, wave breaking, glint, and shadowing, a manual reclassification was required to convert ISODATA results to our final binary dataset (Fig. 2C). Pixels that were unidentifiable, (e.g., whitewash or sun glint) were grouped as unclassified and comprised only a small portion of mosaics (< 2% coverage for 96% of surveys; $n = 69$).

We assess classification accuracy from five mosaics characterized by (1) clear water, (2) turbid water, (3) surf/waves, (4) sunglint, and (5) building shadows respectively, although most mosaics were characterized by clear water. For each mosaic, benthic substrate (rock or sand) at 50 random points were manually annotated and compared to the classified image. The accuracy was determined from the percentage of correctly classified points, yielding an overall accuracy of 88.8%.

3.3. Self-organizing maps (SOMs)

The week-to-week DEMs produced by our surveys display topographic variability that we examine using Self-Organizing Maps (SOMs). SOMs are visualizations of spatially complex datasets produced by a form of unsupervised machine learning that employs artificial neural networks (Parsons and Coats, 2019). The method reveals the evolution of prevailing patterns under specific conditions and times of year by identifying groups of individual DEMs (single surveys) that share similar topographic patterns. These groups (or nodes) are represented by the mean topography of each node (Johnson et al., 2008; Parsons et al., 2018). This is a critical feature of SOMs as other techniques employed in a similar context, such as empirical orthogonal function analysis, may produce spurious spatial structures (Liu et al., 2006; Reusch et al., 2005).

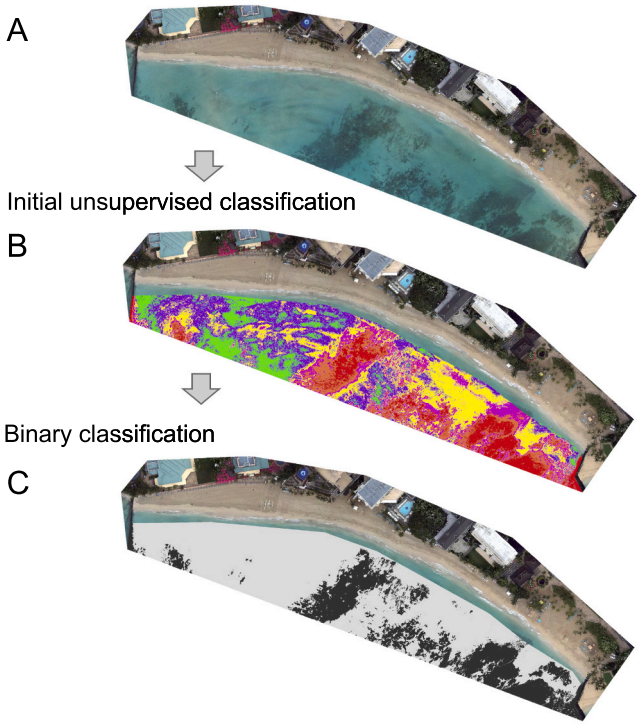

Fig. 2. Nearshore sand cover classification. A. Unclassified RGB photomosaic; B. Unsupervised classification with ENVI 5.4, ISODATA; C. Manual binary classification.

To visualize key topographic features in our 72 DEMs, we employ two SOM analyses. In the first (SOM1), per standard practice (Kohonen, 1990; Johnson et al., 2008), we remove the mean elevation of each grid cell before computing the SOM. For this analysis, we find that seven nodes provide optimal representation of topographic variability—using more than seven nodes resulted in some nodes having only one member, and using fewer than seven nodes failed to capture key variability. In the second analysis (SOM2), in addition to removing the mean elevation of each grid cell, we also remove the mean elevation of the entire beach for each survey. By doing so, this SOM analysis isolates topographic variability independent of changes to beach volume. For SOM2, six nodes were found to best capture the resulting topographic variability, although results were not highly sensitive to this choice. Sequential numbering of these nodes indicates order of similarity. That is, nodes with closer proximity in numbering (1 & 2) are more similar, and those that are further apart in numbering (1 & 7) are more dissimilar (See Fig. 6a and c).

3.4. Physical variables

To identify the principal relationships driving changes in beach volume and width, we collect observations of physical variables (wind, water level, nearshore wave conditions, wave energy flux, and run-up,) that represent local environmental conditions (Fig. 3; see also Appendix A: Sources of physical environmental variables). We compiled hourly wind direction and speed, which were separated based on direction into trade winds (22.5–112.5 DegN; Garza et al., 2012), and westerly winds (200–290 DegN). Measured wind speed within each category was used as wind characteristics. Ocean water level was compiled from Honolulu tide station, and tidal range was defined as the difference between highest and lowest hourly water level each day. Wave characteristics (significant wave height, peak period, and peak direction) produced by an existing SWAN regional wave model (PacIOOS, 2021a) were extracted from a 0.5 × 0.5 km grid location fronting Waikīkī (Booij et al., 1999; Li et al., 2016).

We calculate a proxy for wave energy flux generated by southern hemisphere swell (wave periods: 14–30 s; wave direction: 147–220 DegN) and locally generated trade-wind waves (wave periods: 3–10 s; wave direction: 45–160 DegN; Fletcher et al., 2008). Spectral measurements were obtained from offshore buoys (Supplementary Information). Wave energy flux was calculated for each swell as the energy density in relevant frequency and directional bins of the wave spectrum, multiplied with peak wave period for each timestep. We did not include constants, as we remove the mean for model calculations; this is therefore proportional to the true wave energy flux.

Wave run-up was estimated with an existing empirical equation calibrated specifically for Waikīkī (PacIOOS, 2021b). This equation estimates setup ($su = 0.0655 \cdot H_0$) and infragravity swash ($S_{IG} = 0.275 \cdot H_0$), as a linear function of significant wave height (H_0), and incident swash ($S_{inc} = 0.313 \cdot sl$) as a function of sea level (sl; from MLLW of Honolulu tide station). Run-up is then; $runup = 1.2\left(su + \frac{S}{2}\right)$, where $S = \sqrt{S_{inc}^2 + S_{IG}^2}$.

As there is no *in-situ* data of currents surrounding the Royal Hawaiian Beach, and nearby (~10 km) wave buoys do not sufficiently represent intricate reef currents, a modelling study (De Souza and Powell, 2017) is considered in the discussion. Lastly, we introduce the qualitative notion *quiet conditions* that entails periods of low wind speed (<5 m/s), low water level (at or below MSL) and low wave activity (<0.5 m significant

Fig. 3. Left column, wave characteristics (top to bottom): Significant wave height (m), peak period (s), peak direction (DegN), trade-wind swell energy flux (Wm^{-1}), and south swell energy flux (Wm^{-1}). Right column (top to bottom): Daily average sea level (m), daily tide range (max-min of hourly sea level measurements, m), run-up (m) with a flood elevation threshold of 1.1 m shown in red (PacIOOS, 2021b), wind speed (easterly, ms^{-1}), wind speed (westerly, ms^{-1}). Winds from the west are sparse but, when present, can drive coastal change. (For interpretation of the references to colour in this figure legend, the reader is referred to the web version of this article.)

wave height, and low wave energy flux), for example during the first four months of 2019 (Fig. 3), which appear significant in beach accretion.

3.5. Multiple linear regressions

We use a technique of weighted multiple linear regressions to identify principal drivers of beach change (Anderson et al., 2010; Frazer et al., 2009) (see Extended Methodology). Because of bathymetric complexity related to the adjacent fringing reef, wave characteristics influencing the morphology of the beach display strong alongshore variability. In applying multiple linear regressions, we found poor correlation between physical variables and a representation of the beach in its entirety. Consequently, we identify three physical areas of the beach (east, center, west) for correlation. These beach areas are delineated by two criteria: (1) Topographic structure as reflected in the SOM analyses, and (2) two locations where beach width shows little variation over the study (<5 m vs ± 13 m elsewhere) (Fig. 1). To characterize drivers of change in each segment, we calculate beach volume and average beach width in each segment as predictands and apply the method of multiple linear regressions with physical variables as predictors. All combinations of predictands and predictors ($n = 126$) were evaluated in light of two rules: (1) To eliminate functions with dependent variables. For example, wave energy flux depends on incoming wave height, period, and direction. As a result, wave energy flux was selected as the representative predictor for waves. (2) For each data group (e.g., wind) all related inputs (e.g., easterly wind, westerly wind) were either all included in a regression model, or not (i.e., there is no regression model that uses only easterly winds, without also including westerly winds). The model assumes that all beach variability is represented in the results. The resulting statistically independent relationships were ranked and weighted using an Akaike Information Criterion to identify physical variables most responsible for driving changes in beach morphology (Anderson et al., 2010; Frazer et al., 2009).

4. Results

4.1. Physical variables

Environmental conditions during the study period displayed distinct patterns amongst certain physical variables (Fig. 3): (1) Increases in south swell energy flux show a strong correlation to summer months (Fig. 3e); (2) trade-wind swell energy flux varies throughout the year (Fig. 3d); (3) water levels fluctuate seasonally (Fig. 3f); and (4) tidal range, naturally modulated by the lunar cycle, increases around the summer and winter perigees (Fig. 3g). Other variables display more anomalous behavior, specifically when assessing wave and water level characteristics during the study. Beginning in July 2019, strong and persistent shifts are seen in significant wave height, peak period, and peak direction that are not seen the previous year (Fig. 3a–c). Also beginning in July 2019, trade winds weaken (Fig. 3i), and water level rises 15–20 cm creating an atypical increase that lasts through the end of the calendar year (Fig. 3f).

4.2. Beach observations

4.2.1. Total beach

Beach volume and width for the entire length of Royal Hawaiian Beach ("total") display interannual variability that overprint seasonal signals (Fig. 4a) and that vary compared to individual beach segments (Fig. 4a–d). Over the first 12 months of the monitoring period, total beach volume increased from 12,209 ± 59 m^3 to 14,610 ± 59 m^3 (+20%) until approximately April 2019 when it entered a 10-month period of loss for a net decrease of −690 ± 51 m^3 (−6%; Fig. 4a). Superimposed on these interannual trends, individual loss and recovery events characterize higher frequency variability in beach volume (up to ±10% in one week). Three erosional events in 2018 show correlation with peaks in trade-wind swell energy (Figs. 3d and 4a). Average beach width remains relatively stable over the first year (25.7 to 28.4 ± 0.3 m), but in July 2019 a roughly five-month period of shoreline retreat for an average loss of 5 ± 0.3 m (−18%) is observed (Fig. 4a). The lowest water levels of the survey are seen in February 2019, immediately preceding maxima in total beach volume (14,610 ± 59 m^3; April 2019) and width (28.8 ± 0.3 m; May 2019; Fig. 4a). A Pearson's correlation coefficient was computed to assess the relationship between volume and width. For the entire 22-month period total beach width and volume showed a weak positive correlation ($r = 0.49$ p-value <0.001), which is lower than the correlation values for the individual beach segments, discussed in the following subsections.

4.2.2. East beach

The eastern segment comprises approximately 19% of the total beach, with average beach volume and width of 2400 ± 11.2 m^3 and 23.4 ± 0.3 m respectively. Large (up to ±26%) changes are observed between weeks (Fig. 4b). Notably, between October 2018 and March 2019 beach volume increased by 52% and then returned for a net loss of −6% by the end of observations. Beach volume and width in the eastern segment showed relatively strong correlation ($r = 0.73$ p-value <0.001), with variations in volume typically preceding variations in width. The east segments responded strongly to Kona conditions, for example a 7 m increase in beach width followed a strong southwesterly Kona storm in February 2019.

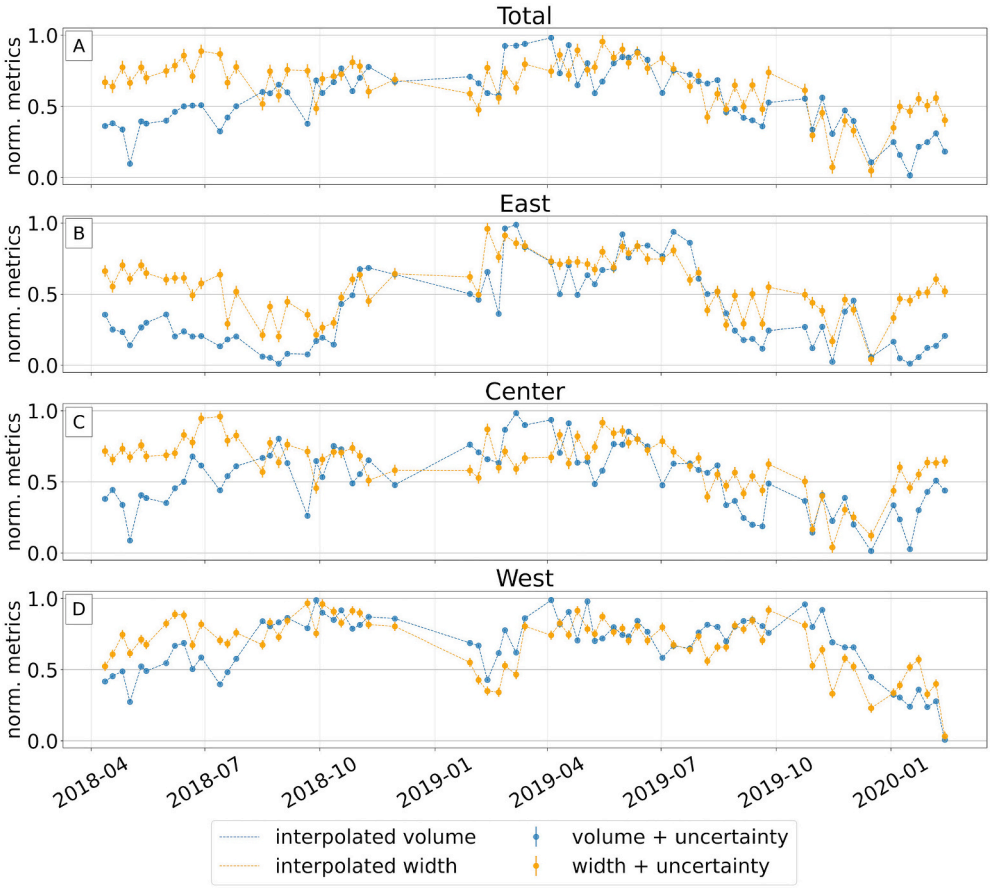

Fig. 4. Normalized (0–1) beach observation (circles + uncertainty) and linear interpolation (dashed line) for volume (blue) and width (orange) for the total beach, and segments east, center, and west over the two-year survey period. (For interpretation of the references to colour in this figure legend, the reader is referred to the web version of this article.)

4.2.3. Center beach

Sand volume in the center segment closely tracks the beach as a whole, showing 12 months of accretion followed by 10 months of loss (Fig. 4c). However, unlike the other beach segments, no net decrease is observed. The center segment averaged 6836 ± 28 m^3 (52% of total beach volume), with an average beach width of 27.7 ± 0.3 m. Individual volume loss and recovery events create larger relative changes compared to those for the total beach (Fig. 4c; blue). Short-lived beach width loss and recovery events (± 5% or approx. ± 1 m) characterize the entire survey period, although during the first 12 months there was little net change (Fig. 4c; orange). The correlation between width and volume is low ($r = 0.50$ p-value <0.001), and variations in width are generally asynchronous with volume.

4.2.4. West beach

The west beach segment is the widest (average 28.6 ± 0.3 m) and makes up 28% of the beach volume (average 3665 ± 15 m^3). Over the first seven months of monitoring, sand volume showed a net increase of 21% through November 2018 (Fig. 4d; blue). When observations resumed nine weeks later, this increase had been lost, but returned again by April 2019 and remained relatively constant through the following summer and fall. By November 2019, sand volume dramatically decreased by 35% and remained unchanged until February 2020 when observations ended (Fig. 4d; blue). Overall, beach volume decreased by 20% during the course of the study, with beach width following a similar history as quantified by a high correlation value ($r = 0.65$ p-value <0.001; Fig. 4d).

4.3. Nearshore sand cover

In order to improve our understanding of how changes in nearshore sand cover correlate to changes in the adjacent beach, we identify three segments of the sand field that correspond to the east, center, and west beach segments (Fig. 1). During the 22 months of observation, percent nearshore sand cover displayed both high frequency variability as well as interannual trends across all three segments (Fig. 5).

The east sand field, which is generally shallowest and contains the greatest amount of rocky substrate, displayed two distinct interannual trends with superimposed high frequency (weekly) fluctuations (Fig. 5; blue). A general phase of sand cover expansion (from 40 to 60% sand cover) marked the first 11 months of the study (Fig. 5; blue). Beginning in March 2019 and extending to the end of the survey, percent sand cover decreased, ultimately yielding no net change.

The center sand field is characterized by a large rocky outcrop located east of the fringing reef channel (Fig. 1). At times, fluctuations in sand cover reduce the surface area of this rocky region as much as 50%. Overall, total percent sand cover in the center sand field ranged from 50 to 85% (Fig. 5; orange). Following an initial decrease in sand cover that ended in August 2018, a slow but persistent expansion peaked in the spring of 2019. Subsequently, percent sand cover showed multi-month trends of expansion and contraction to the end of the survey period.

The west sand field contains the highest proportion of sand in the study area, with only a few areas of rocky substrate (Fig. 1). These become buried during periods of high sand cover. Although highly variable, sand cover generally decreases from 95% to a minimum of 70% midway through the study, before recovering by the end of the observation period (Fig. 5; green).

The relative pattern of sand cover variability in the east and west sand fields strongly suggest that they exchange sand (Fig. 5; green, blue). Three distinct phases characterize the study period: (1) From April 2018 to January 2019 the eastern sand field shows a slow increase in sand cover while the western sand field, although stable in the early months, ultimately loses about 10% of its sand cover over the same period; (2) from January to April 2019, both sand fields stabilize at 70–80% sand cover; (3) From April 2019 to the end of the study, the eastern sand field loses 20–30% of its sand cover returning to original values, while the western sand field regains the 10% sand cover it had lost in phase 1 (Fig. 5).

4.4. Self-organizing maps (SOMs)

Here, we present results from the SOM analysis, a form of neural network cluster analysis, to identify and group individual DEMs (single surveys) with similar topographic patterns. Note that clusters (also termed nodes) close in numbering (e.g., 1 and 2) are more topographically similar than clusters further apart. Below we describe the dominant topographic patterns revealed by both SOM analyses.

4.4.1. SOM1

We show that when the mean elevation for each cell is removed (SOM1) there are 7 beach topographic structures (Fig. 6a), and that node assignment through time strongly resembles variations in beach volume (Fig. 6b). Over the entire study period, higher numbered nodes correspond to periods of high beach volume, and lower numbered nodes to low beach volume (Fig. 6b). Nodes 1 and 7 correspond to volume minima and maxima (resp.) and share an area of higher elevation in the center (Fig. 6a). During volume minima (node 1) elevation is low to the east and west, suggesting these are areas of erosion (Fig. 6a). Nodes 4 and 5 correspond to phases of increasing volume to the east and west through 2018, indicating that accretion starts on either side of the

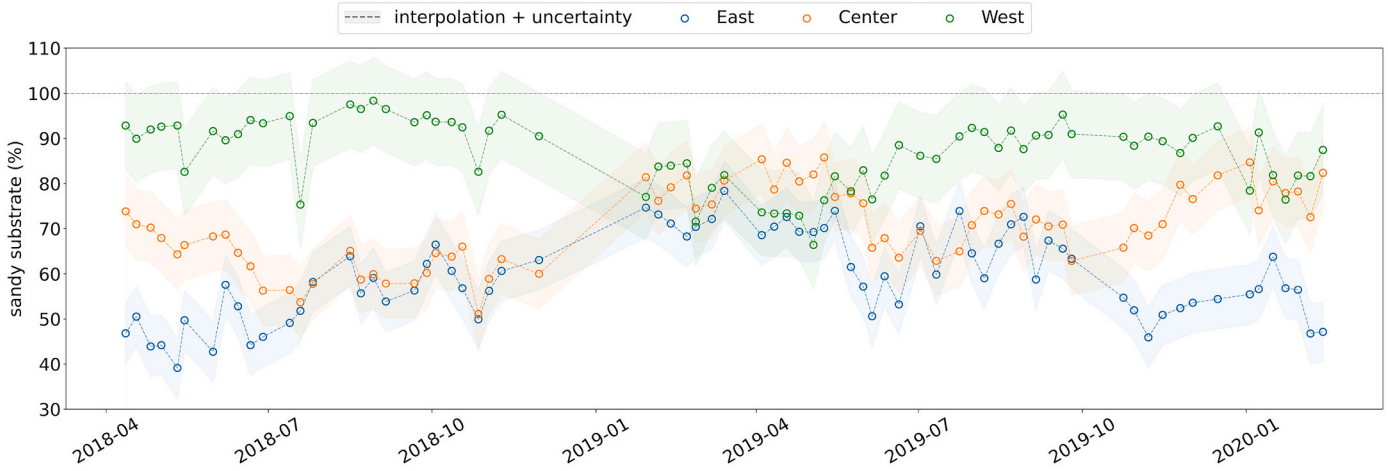

Fig. 5. Nearshore percent sand cover adjacent to east, center, and west beach segments. Circles, representing individual surveys, are linearly interpolated (dashed line). Shading represents quantified error (11.2%).

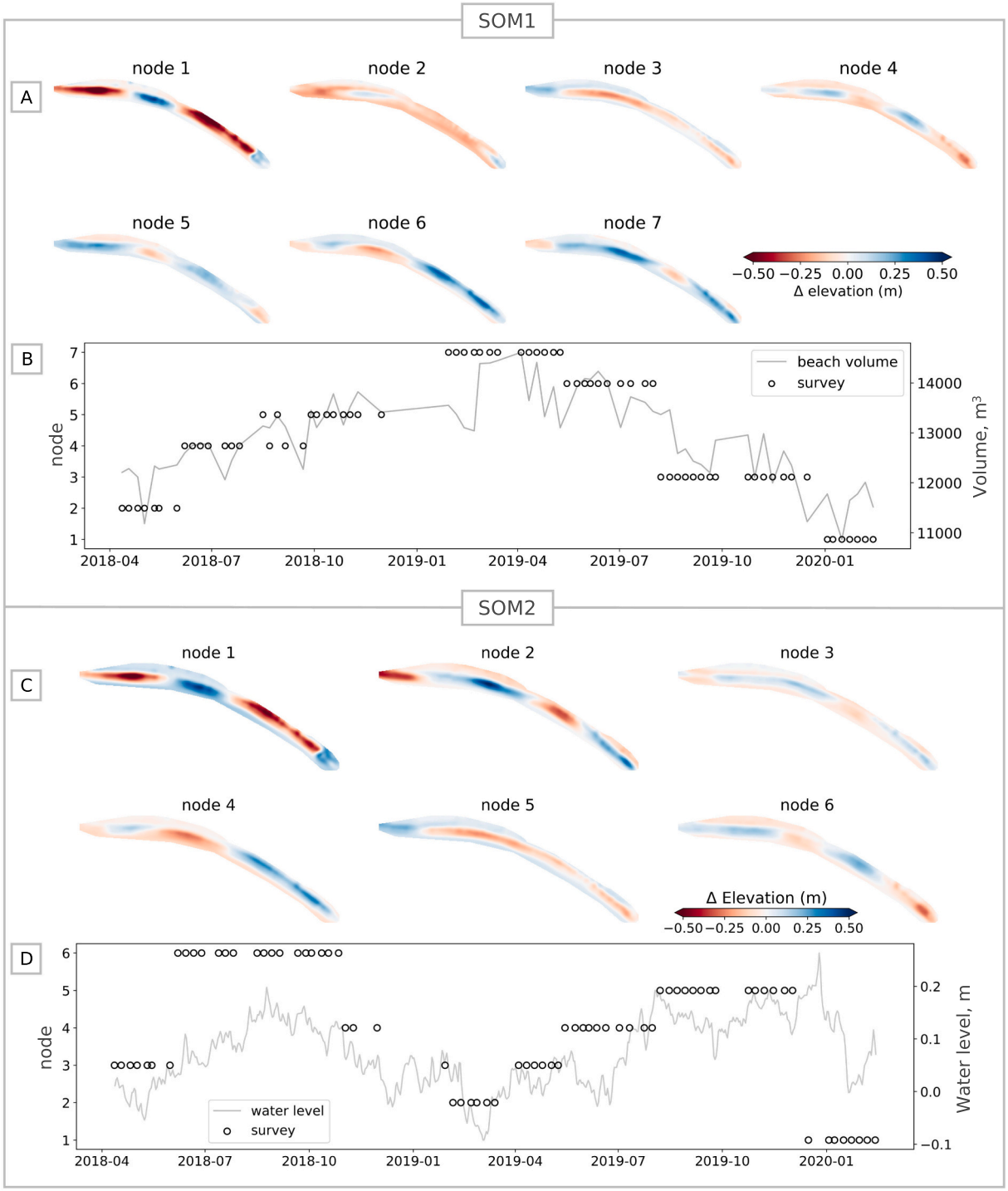

Fig. 6. Results from two analyses using SOMs. For each analysis (a and b) DEMs illustrate the mean topography of each node. Plots accompanying a and b show individual surveys (open circles) assigned to each node (left axis) in chronological order (horizontal axis). a) SOM1 individual survey and node chronology resembles beach volume changes (right axis, m^3). b) SOM2, individual and node chronology reveals a seasonal pattern, plotted with water level (right axis, m).

nearshore channel and expands throughout the accretion phase (to node 5, then 7). Nodes 6 and 3 describe the erosional period July to December 2019 when beach volume and width decreased. These nodes suggest that erosion originated in the center (node 6), and expanded eastward (node 3).

4.4.2. SOM2

When the mean elevation of each survey is removed (SOM2), thereby removing effect the of beach size (Fig. 6c and d), six nodes represent topographic variability and show a strong seasonal influence. Nodes 1–3 correspond with winter and spring and nodes 4–6 with summer and fall (Fig. 6d). This implies that variations in beach topography retain a seasonal structure although changes in beach volume (Fig. 6a) do not. Nodes 4 and 3 operate as transitional topographic signatures between summer and winter end states (Fig. 6d).

Although node assignment displays seasonality, there are also year-to-year differences (Fig. 6d). For both 2018 and 2019, sand is relatively evenly distributed in the late spring (April; node 3), just before

summer south swell arrives. The summer of 2018 display four alternating cells of higher and lower elevation respectively (node 6), while summer of 2019 lack the two eastern alternating cells and generally display an even low topography throughout the center and east (node 5). Differences in environmental conditions and prior beach state can be attributed to these differences in topography.

4.5. Regression analysis

Using multiple linear regressions, we establish the strength of correlation-based relationships between physical environmental parameters (swell, wind, water level) and indicators of beach response (volume, width), to determine the dominant drivers of beach morphologic change (Table 1; multiple regression). We find that water level and wave energy are important drivers for all beach characteristics, despite large variability in primary drivers across beach segments and in volume compared to width (Table 1; multiple regression). Beach volume and width are described separately below. Using these relationships to model predictions of volume and width for the east, center, and west beach segments, we capture short-term as well as interannual variability (Fig. 7). Additional single linear regression models were used to: (1) identify correlations between beach indicators (volume and width) and the development of the three sand fields located immediately offshore, and (2) investigate correlations between single physical drivers and beach responses (Table 1; single regression).

4.5.1. Beach volume

We find that changes in beach volume are nearly equally responsive to water level variations (36.1%), wind conditions (28.0%), and wave energy flux (35.9%) (Table 1; multiple regression). Variations in water level show the strongest influence on seasonal beach volume variability (Fig. 3f). Low water levels in winter months (generally <0.05 m above MSL) correspond to beach volume increases while high water levels during summer (>0.1 m above MSL) correspond to beach volume losses (Figs. 3 and 4). High water levels correlate to volume loss from the east and center beach segments, and volume gains in the western beach segment (Table 1; multiple regression), indicating that elevated water levels facilitate longshore sediment transport. Tidal range varies bimonthly with the lunar cycle and there is a correspondence of beach volume loss to tidal range increases particularly in the west segment.

Wind characteristics explain approximately one fourth of the observed variability in beach volume (Table 1; multiple regression). Strong winds (> 10 m/s) from the east (hereafter “trade winds”) correspond to beach volume losses across all segments, with larger erosion in the east and smaller erosion in the west. Westerly winds correspond to volume increases at the center and west beach segments, while the effect on the east beach segment is ambiguous in showing small decreases (<5% explained) in the multiple linear regressions and small increases in single linear regressions (Table 1).

Wave energy flux shows strong correlation to changes in beach volume (35.9%; Table 1; multiple regression). Increases in south swell energy flux correspond to volume gains at all beach segments and is the dominant control for the west beach segment (Table 1; multiple regression). The east and center beach segments show pronounced erosion, and the west beach segment pronounced accretion, as a result of increases in trade-wind swell energy flux.

Using single linear regressions to improve understanding of sediment dynamics between the subaerial beach and nearshore, we find strong correlations between beach segments and non-adjoining nearshore segments. For example, the west sand field is inversely correlated with beach volume at the east and center beach segments (Pearson's correlation coefficient; $r_{east} = -0.48$ p-value <0.001; $r_{center} = -0.33$ p-value 0.004 resp.), suggesting that alongshore sediment exchange occurs between the west sand field and the center/east beach segments. Positive correlations were observed between the east sand field and the east, center, and west beach segments ($r_{east} = 0.45$ $r_{center} = 0.40$, $r_{west} = 0.40$, p-values <0.001, resp), indicating that increases in the east sand field are contemporaneous with increased beach volume at all three beach segments. Apart from the east segment, adjoining pairs of subaerial and nearshore beach segments (e.g., west beach and west sand field) did not show significant correlations, suggesting cross-shore sediment transport is limited. However, these correlations reveal that sand exchange with the shallow sea floor in front of Royal Hawaiian Beach is a critical aspect of littoral processes.

4.5.2. Beach width

Changes in beach width are driven by water level variations (39.7%), wind conditions (32.0%), and wave energy flux produced by south and trade-wind swell (28.3%) (Table 1; multiple regressions). Overall, the multiple linear regression model finds stronger correlations to changes in beach width than to changes in beach volume (Fig. 7). Additionally, it does a good job of representing weekly responses in beach width that correspond to the tidal cycle and to peaks in wave energy flux (Fig. 7).

High water levels, and tidal range, correspond to beach narrowing at all beach segments (Table 1; multiple regressions). Notably the influence of water level variations is seven times higher for the east segment (52.8%) compared to the west segment (7.4%).

South and trade-wind swell energy explain 21.5 and 14.5% of beach

Table 1

Results showing environmental variables (column 1), group name (column 2), and parameter time series averaging window (column 3). Columns 4–9 show Pearson correlation coefficient from single linear regressions for environmental parameters and beach indicators. Bold indicates significant relationships (p-value <0.05). Columns 10–17 show results of the multiple linear regressions model (see Extended Methodology), indicating the proportion (%) of change explained by each variable for the east, center, west, and total beach. Positive (negative) values indicate an increase (decrease) in beach volume or width resulting from an increase in an environmental variable. Filter*: A weighted average filter, in which weights decay exponentially over time (see Extended Methodology).

			Single regressions: 1:1 Correlation coefficient						**Multiple regressions: Proportion explained (%)**							
			Volume			*Width*			*Volume*				*Width*			
Variable	Group	*n days*	East	Center	West	East	Center	West	East	Center	West	Total	East	Center	West	Total
Energy flux south	swell	Filter*	0.15	0.15	**0.32**	0.03	**0.36**	**0.59**	12.7	15.6	36.1	21.5	6.6	17.3	32.7	18.9
Energy flux trades	swell	Filter*	**−0.29**	**−0.31**	0.10	**−0.24**	**−0.26**	0.09	−11.4	−17.8	14.2	−14.5	−10.2	−5.1	12.8	−9.4
Wind speed West	wind	50	**0.57**	**0.37**	0.07	**0.56**	0.12	−0.19	−4.2	5.0	10.2	6.5	5.2	14.8	13.7	20.8
Wind speed East	wind	50	**−0.66**	**−0.30**	−0.12	**−0.43**	0.17	**0.30**	−38.9	−15.0	−10.7	−21.5	−15.1	24.9	22.3	11.2
Water Level	water	30	**−0.56**	**−0.50**	0.09	**−0.78**	**−0.58**	−0.08	−24.1	−33.4	11.1	−22.9	−52.8	−31.1	−7.4	−30.4
Tidal range	water	7	−0.13	−0.13	**−0.24**	−0.16	−0.13	**−0.24**	−8.3	−12.8	−17.6	−12.9	−10.1	−6.7	−11.1	−9.3
Run-up	water	7	−0.10	**−0.26**	0.03	**−0.23**	−0.07	**0.30**	0.4	−0.5	−0.2	−0.4	0.0	0.0	0.0	0.0
Total									100.0	100.0	100.0	100.0	100.0	100.0	100.0	100.0

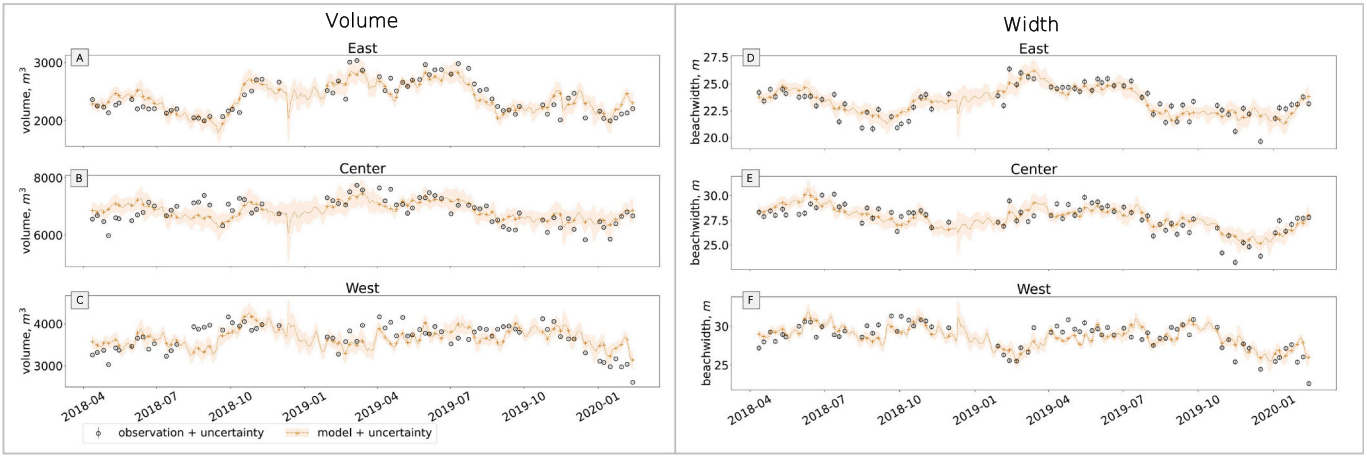

Fig. 7. Multiple linear regressions model (orange line + uncertainty) of beach volume for east (a), center (b), and west (c) and beach width for east (d), center (e), and west (f). Survey data (black circles + uncertainty); model data for survey dates (orange '+').

width variations respectively (Table 1; multiple regression). The west segment is most responsive to swell energy (50.3% combined). A seasonal signal is recorded in the south swell energy flux (Fig. 3e), with increases during summer months (Fig. 3e) corresponding to beach widening at all segments. Trade-wind swell energy, on the other hand, corresponds to beach widening at the west beach segment and narrowing in the center and east beach segments.

Variations in wind drive changes in beach width, although this influence is strongest in the central and west beach segments (Table 1; multiple regression). During times of strong trade winds, the west and center beach segments widen while the east beach segment narrows. Winds from the west drive widening across the entire beach, and most strongly at the center (Table 1; multiple regression).

Strong correlations also exist between beach width and variations in the nearshore sand field. The center sand field is inversely correlated to changes in width at the center and west beach segments (Pearson correlation coefficient; $r = -0.27$ p-value $= 0.021$; $r = -0.50$ p-value <0.001, resp.), suggesting that sediment gain (or losses) in the center sand field are coincident to sediment losses (or gain) at the west/center beach segments. Amongst the nearshore sand fields, we find that the east and center sand fields change in unison ($r = 0.42$, p-value <0.001) but are negatively correlated to variations in the west sand field ($r = -0.39$; $r = -0.58$ respectively; p-values <0.001; Fig. 5).

5. Discussion

Weekly sUAS monitoring coupled with traditional ground surveys of key beach features provides a unique high-resolution dataset to improve understanding of fundamental coastal processes governing the stability of the reef-fronted Royal Hawaiian Beach. Specifically, using multiple (and single) linear regressions, SOMs, remote sensing, and existing nearshore wave and runup models, we identify: (1) key relationships driving changes in beach volume and width, (2) seasonal variability, and (3) sediment sources and sinks under specific wave, wind, and water level conditions. These findings are discussed in the sections below.

5.1. Drivers of beach change and alongshore variations in beach response

The principal drivers of beach change include water level variability, wave energy flux from south swell and trade-wind swell, and 50-day averaged wind conditions (Table 1). Accretion is generally driven by south swell energy flux, while elevated water level and increased trade swell energy flux enhance alongshore sediment exchange toward the northwest (Table 1). There is no single driver that explains beach variability for all segments, as alongshore differences in reef submergence, bottom roughness, and orientation create unique conditions under which the individual beach segments respond to forcing (Tables 1 and 2).

The east beach segment has the shallowest nearshore region (Habel et al., 2016) of the three and is influenced most strongly by water level variations. Compared to the west segment, water level in the east carries seven times more influence in driving changes in beach width and two times more in driving changes in beach volume (Table 1). Small differences in reef submergence level can strongly amplify or suppress wave energy transfer across the reef (Péquignet et al., 2011; Siegle and Costa, 2017). De Souza and Powell (2017) modeled waves and currents of Waikīkī and found that because the east nearshore segment is shallower it experiences a larger set-up than surrounding nearshore areas, which leads to a divergence of wave energy – and sediment – that flow into the central beach. Here, we show that a beach fronted by very shallow reef is associated with strong erosion in response to even small (cm's) increases in water levels, possibly as a result of increased wave energy, setup, and divergence. By contrast, Baldock and Ginzo (2020) found that for specific reef-fronted or lagoon fronted-beaches, small water level increases may lead to beach accretion, and (Risandi et al., 2020) observed the largest beach accretion of a reef-fronted beach in

Table 2
Important physical processes that drive beach change, and related responses in beach and nearshore sand bodies.

	Drivers	Responders	
		Sand receivers (+)	Sand soures (−)
1	**Low wind trade conditions**	West beach & sand field	East beach & sand field Center beach & sand field
2	**High wind trade conditions**	West sand field	East beach & sand field Center sand field
3	**South swell energy flux**	East beach Center beach West beach & sand field	East sand field Center sand field
4	**High water levels & South swell**	West beach & sand field	East beach & sand field Center beach & sand field
5	**High water levels & other waves**	West sand field	East beach & sand field Center beach & sand field West beach
6	**Kona storms**	East beach & sand field	West beach
7	**Quiet conditions**	East beach Center beach West beach	–
8	**Westerly winds**	East sand field Center beach & sand field West beach	West sand field

Australia concurrent with high water levels. These findings highlight large variability of reef-fronted beaches and the need for site-specific monitoring.

We find that for a beach segment bounded by a down-current groin, such as the west beach segment (Fig. 1), wave energy has the greatest influence on beach changes, with higher wave energy generally corresponding to width and volume gains. Wave energy may suspend sediments, which are then transported in the dominant current direction (northwesterly; Gerritsen, 1978), where they accrete against the western groin. The west beach has the lowest proportion of rocky outcrops (Fig. 1), thereby allowing more breaking wave energy to reach shore, suspending more sediment.

The center beach does not respond to one exclusive driver. Variations in width correlate strongest to wind conditions, whereas wave energy drives the largest changes in volume. A deeper sand channel is located at the center beach, where offshore currents of 1 m/s have been modelled (De Souza and Powell, 2017). Past research suggests that this channel functions as a sediment sink during the winter months and a source during the summer months (Gerritsen, 1978; Habel et al., 2016), consistent with our findings, as discussed further in 5.3.2.

5.2. Seasonal change

Interannual processes of erosion and accretion overprint seasonal change in both volume and width. Preceding studies of beach morphology in Hawai'i have found strong seasonal structure in both shoreline position and beach volume (Dail et al., 2000; Eversole and Fletcher, 2002; Norcross et al., 2002). Habel et al. (2016) found that both seasonal and interannual changes characterized Royal Hawaiian Beach, Waikīkī, following a beach re-nourishment project in 2012. These studies attribute seasonal characteristics to the typically strong seasonal wave climate (Vitousek and Fletcher, 2008) of Hawai'i. During the period of our study (Apr 2018–Feb 2020), physical environmental parameters displayed seasonal trends primarily in south swell energy flux, but water level and trade conditions began an unusual increase during the last half of 2019, perhaps yielding stronger interannual variability in our observed beach characteristics (Fig. 3).

Analysis using SOMs revealed that beach topography, (i.e., where sand is distributed regardless of beach size) retains a seasonal structure. This is generally characterized by lower sand accumulation at the center and higher in east and west during summer months (May–September), which reverse during winter months. Studies elsewhere found seasonal rotation of reef-fronted pocket beaches (Jeanson et al., 2013; Risandi et al., 2020), consistent with the SOM2 analysis (e.g. node 6 with alternating high and low elevation; Fig. 6c). Segura et al. (2018) identified both seasonal and interannual (El Niño / La Niña) variations of shoreline position modulated primarily by water level. This study suggests that seasonal changes to volume and width are not dominant, perhaps due to interannual variations in environmental drivers, but that beach topography does retain a seasonal structure.

5.3. Connections between subaerial and nearshore beach

We identified eight conditions that drive unique sand sharing patterns between subaerial beach segments and the nearshore sand fields (summarized in Table 2). The relationships were derived from regression analysis (Table 1) and SOMs (Fig. 6) by identifying beach segments and sand fields that gain or lose sand under specific conditions. The relationships were then verified in observed data and physical variables (Figs. 3 and 4). The eight driving conditions are Trade conditions (low and high wind speed), South swells, Kona storms, quiet conditions (see Section 2.3), Westerly winds, and High water levels (during South swell and during other waves). Below we describe typical conditions driving sand exchange amongst subaerial and nearshore beach segments.

5.3.1. Trade conditions

Trade conditions, including trade-wind swell energy flux and easterly trade winds, generally drive alongshore sediment transport from east to west (Table 1). This has been established in preceding studies (Gerritsen, 1978; Habel et al., 2016; Miller and Fletcher, 2003). However, here we differentiate between (1) low wind speed trades and (2) high wind speed trades. Low wind speed trades drive strong alongshore sediment exchange: The west subaerial beach segment widens, and submerged sand field expands, while the east and center beach segments narrow, and their adjacent sand fields lose sand (Table 2). High wind speed trades, on the other hand, drive accelerated erosion on the east beach segment and sand field, and reduced accretion to the west beach segment and sand field. The center segment responds by widening but also losing volume, which may reflect the influence of wave driven circulation and setup, such that offshore flow interrupts the alongshore delivery of sediment from the east to the west by pushing sand out into the channel.

A study examining influence of persistent sea breezes on a reef-fronted beach in Australia found a 50% reduction in sea breeze led to a 50% reduction of alongshore sediment transport (Gallop et al., 2011). Our findings support that a significant reduction in trade-winds (or sea breezes) reduce alongshore exchange, but also find that a significant increase in wind speed disrupts nearshore currents and longshore delivery of sand. By contrast, locally generated wind waves were observed as the primary mechanism of erosion as even large cyclone swell energy were dissipated across the reef (Cuttler et al., 2018). In general, we find local wind speed and wind waves play a critical role in beach morphology (and explain 36 and 30% of change in volume and width resp.; Table 1), but notable differences emerge in beach and nearshore response to low wind speed compared to high wind speed trades.

5.3.2. South swell energy flux

Strong south swell corresponds with increases in volume and width in all beach segments. Decreases in the east and center sand fields suggest that these function as sediment sources for the entire beach (Tables 1 and 2), while the west sand field increases, possibly due to sediment buildup against the terminal groin. Considering volume gains of Royal Hawaiian Beach, it is likely that the central sand channel functions as a conduit for sand delivery, where south swell mobilizes and delivers sand from offshore sources. This interpretation supports the findings of Conger et al. (2005), that sand channels in carbonate beach environments in Hawai'i connect offshore and nearshore sediments. It also adds to the existing consensus that southern hemisphere storm swells promote accretion of Waikīkī beaches (Habel et al., 2016; Miller and Fletcher, 2003). For other beaches in Hawai'i, Norcross et al. (2002) found that a large storm swell was responsible for accretion while Dail et al. (2000) found that strong swells are associated with erosion. While this study adds to the consensus that nearshore channels provide a mechanism for sediment transport onto Waikīkī beaches, local geologic setting appears to be a dominant control on beach response to swell energy flux.

5.3.3. High water levels

Elevated water levels facilitate alongshore sediment transport by eroding the east and center subaerial beach segments and submerged sand fields, while building the west beach and sand field (Table 2); a similar influence to that of trade conditions. Because water levels modulates wave energy that reaches shore (Gourlay and Colleter, 2005; Péquignet et al., 2011), it is important to consider water level impacts under a range of wave activity. We differentiate between high water levels during (1) increased south swell energy flux, and (2) other types of wave activity. For both, the center and east beach segments erode. The difference exists in where this sediment is deposited: When high water levels are coincident with increased south swell energy flux, the west beach segment and sand field builds, but when coincident with other types of waves (e.g., October 2019), the west beach segment does not

build, and there are no clear increases occurring elsewhere in the nearshore, suggesting offshore deposition. As mentioned previously, past studies have found elevated water levels associated with erosion (Anderson et al., 2015; Romine et al., 2013) and accretion (Baldock et al., 2015; Risandi et al., 2020) of reef-fronted beaches. Here, we find high water levels are associated with (1) increased alongshore sediment exchange, supporting the findings of Grady et al. (2013), and (2) exacerbated erosion of the east beach segments fronted by a very shallow fringing reef.

5.3.4. Kona storms

From raw observations we find that southwesterly Kona storms reverse the direction of alongshore currents and drive sediment from west to east. Following a strong westerly Kona storm in February 2019, we observed a 7 m increase in beach width on the east beach segment. At the west beach segment, a ~ 1 m high erosional scarp formed. This supports previous findings by Miller and Fletcher (2003), that Kona conditions resulted in erosion at the west segment along with a reversed sediment transport direction.

5.3.5. Quiet conditions

Quiet conditions, defined as periods of low wave activity, low water levels, and relatively slow winds, appear significant in beach accretion. Between January and May 2019, where quiet conditions are present, we observed accretion at all beach segments, and little change in the nearshore sand fields. During this period, beach volume and width maxima were reached by April and May 2019, respectively (Fig. 4), suggesting that quiet conditions are favorable to overall beach accretion.

5.4. Profile response

We found that beach profile evolution was largely symmetric, meaning that onshore and offshore portions of the profile gained (or lost) sand simultaneously during episodes of accretion (or erosion). This is contrary to the standard beach morphologic response model described by Wright and Short (1984). Their model describes a cross-shore reduction in slope associated with high energy, wave driven profile erosion (Wright and Short, 1984). A standard dissipative morphology consists of an offshore sandbar composed of sand eroded from the foreshore region that shallows the seafloor sufficiently to cause wave energy dissipation. As wave energy wanes, the sandbar migrates landward creating a series of shallow surf zone features and eventually accretes onto the foreshore. This steepens the profile marking a standard reflective morphology. However, beach profiles within our study area did not present the fundamental characteristic of onshore loss (gain) balanced by offshore gain (loss), which we refer to as profile asymmetry.

Instead, we discovered asymmetry in the longshore component of our observations. For example, trade conditions drive sediment loss from the east segment (subaerial beach and submerged sand field) and sediment gain in the west segment of Royal Hawaiian Beach. Similarly, Kona winds drive sediment loss in the west and gain in the east. Norcross et al. (2003) examined a cross section of representative beach systems in Hawai'i and found in all cases that longshore transport dominated seasonal beach development despite the study sites being located in different meteorologic and oceanographic settings. Similar alongshore sediment transport has been observed in previous studies of Hawai'i beaches (Eversole and Fletcher, 2002; Norcross et al., 2002; Norcross et al., 2003), as well as on other reef-fronted beach systems including in Australia (Gallop et al., 2013; Risandi et al., 2020; Segura et al., 2018) and the Indian Ocean (Jeanson et al., 2013). These studies identified alongshore zones that alternate in seasonal erosion and accretion patterns, usually with headlands as nodal points where longshore transport is hindered. At the Royal Hawaiian Beach, no distinct nodal point exists, but alongshore zones are clearly indicated by alternating erosion and accretion (for example between east and west). From this, we conclude that although aspects of the standard model such as profile steepening and short-term cross-shore sediment transport are found on Hawaiian beaches (Habel et al., 2016), researchers should not assume that profile asymmetry controls reef-fronted beach morphology.

5.5. Implications for management in a changing climate

We find that trade conditions and water level variability modulate wave energy across the fringing reef surface. These processes work in conjunction with other physical parameters (e.g., swells, wind-generated waves, and currents) to drive sediment exchange and therefore constitute fundamental conditions governing beach stability. As such, factors influencing short-term and long-term water level variations, as well as trade conditions, should be closely considered by beach managers. These may include, for example, maximum spring tides (king tides), the El Niño-Southern Oscillation (ENSO), and long-term sea level rise.

High-tide flooding is present in Honolulu during summer perigee king tides and can result in wave overwash of the coastline, beach erosion, and disruptions to local economic activity (Banno and Kuriyama, 2020; Hino et al., 2019). The frequency of high-tide flooding is found to precipitously increase around the mid-2030s as a result of long-term sea level rise and nodal cycle modulations of tidal amplitude (Thompson et al., 2021). The number of days where high tide exceeds 35 cm above MHHW plateaus at 40–45 days/year until the year 2035. A dramatic increase to 152 days/year is predicted by 2040, and 254 days/year by 2045 for RPC8.5 (Thompson et al., 2019). These increases of high-tide flooding events mean more short-term high frequency episodes of deepening across the fringing reef, thus allowing increased wave energy flux impacts and associated sediment movement.

The ENSO cycle has been linked to distinct coastal responses (Barnard et al., 2015; Barnard et al., 2017; Vos et al., 2021), and identified as a primary reason for interannual variability in water level – and shoreline position – for a reef-fronted beach in Australia (Segura et al., 2018). Wind and water level conditions in Hawai'i are also modulated by ENSO (Barnard et al., 2015; Vos et al., 2021). Increases in extreme El Niño events are projected for the coming decades (Cai et al., 2014), although there is uncertainty in these projections (Stevenson et al., 2021). If these projections are correct, local El Niño impacts like low trade conditions, increased swell energy, and elevated sea surface temperature would become more common. Strong El Niño events are also associated with a delayed (1–2 years) increase in ocean water level as water level anomalies propagate westward as a Rossby wave, as observed following the 2015 El Niño (Long et al., 2020). By contrast, La Niña events are associated with strong trade conditions. The frequency of extreme La Niña events has also been projected to increase, doubling in frequency by 2100 (Cai et al., 2015). La Niña events, in triggering strong trade conditions, can be expected to generate beach erosion and loss. But the resulting increase in alongshore sediment transport may generate accretion to the west depending on underlying environmental conditions.

As stated earlier, the Honolulu tide gauge shows a recent increase in the rate of SLR (historical, 1900–2020: 1.5 mm yr^{-1}; recent, 2000–2020: 3.5 mm yr^{-1}). This is consistent with projections of accelerating global mean sea level rise (historical, 1900–1990: 1.4 mm yr^{-1}; recent, 2006–2015: 3.6 mm yr^{-1}; IPCC, 2021). Although SLR has inherently long timescales, it amplifies the impacts of higher frequency events like king tides and ENSO-related water level variability. Critically, SLR may not be mitigated by reef accretion because of the negative influence of ocean acidification and high sea surface temperature (Hoegh-Guldberg et al., 2007; Pandolfi et al., 2011). Radiocarbon dating of reef structures in Hawai'i identifies the fringing reef as a fossil structure formed approximately 2000 yrs. BP (Grossman et al., 2006), further suggesting that because of inimical nearshore conditions, the reef may not accrete under SLR. Managers should thus anticipate that SLR will increase water depths over the fringing reef leading to higher wave energy and sediment movement in the beach and nearshore area that can accelerate

erosion.

Over the course of the study, we observed that elevated water levels likely reduced beach recovery following high energy events. For example, during summer and fall of 2018 (May–October), three episodes of trade-wind swell resulted in significant beach loss, which was fully recovered within one week. However, during the fall of 2019, coincident with an atypical elevated water levels, the beach did not recover from similar peaks in trade-wind swell energy. This resulted in the observed beach volume falling below the initial survey volume. The period was also characterized by increased nearshore wave activity despite there being no measured increase in swell energy (Fig. 3a–c). This suggests that (1) beach recovery may be hindered by high water levels and (2) seasonal and interannual water level increases may drive amplified beach erosion (Abessolo et al., 2020; Segura et al., 2018; Theuerkauf et al., 2014). If true, and given that water levels will continue to rise, Royal Hawaiian Beach may be less resilient in the future.

6. Conclusions

Weekly surveys of a reef-fronted beach system coupled with image classification of nearshore sand fields provide insight into unique sand source-sink networks that vary under a range of environmental conditions. Generally, individual beach segments and their adjacent sand field gain and lose sand in unison, which differs from the standard reflective/dissipative beach model. Alongshore transport dominates sediment dynamics and environmental conditions, such as elevated water levels, trade conditions, and Kona storms, enhance this alongshore sediment exchange. The primary environmental drivers of beach change are water level variability and wave energy flux. Bathymetric complexity related to the adjacent fringing reef causes alongshore variability in beach response. Further analysis using SOMs suggests that beach topography retains a seasonal structure, although changes in beach volume reflect interannual variability.

This work improves understanding of sediment dynamics and complex beach responses to environmental conditions on a reef-fronted beach. Our results suggest that a future characterized by SLR and amplified ENSO events may accelerate erosion and contribute to destabilizing the Royal Hawaiian Beach, and possibly geologically similar beach systems, and thus managers should expect increased cost of beach maintenance in the future.

Data availability

Environmental data used in this study is available from links provided in the Supplementary Information; Sources of physical environmental variables. Processed survey data products are available from Mendeley Data Repository (doi:10.17632/9nz8gsj7tx.1).

Declaration of Competing Interest

The authors in this paper declare no conflicts of interests.

Acknowledgements

This work was supported by the City and County of Honolulu Office of Climate Change, Sustainability and Resiliency and The Office of Naval Research. A publication of the Hawai'i Office of Planning, Coastal Zone Management Program, pursuant to the National Oceanic and Atmospheric Administration Award No. NA17NOS4190171. S.C. was supported by NASA award 80NSSC20K1241. This is SOEST contribution 11483.

We graciously thank M. Guilles and C. Tognacchini for advice in wave run-up assessments for Waikīkī, and P. Thompson for guidance on sea level change. The authors thank N. Li for helpful discussion of the SWAN nearshore wave model output and D. Eversole for valuable insights of Waikīkī beaches. We are grateful for invaluable assistance with field work from K. Tavares, N. Kannegiesser, K. McDonald, K. Wong, C. Creadick, and J. Kalksma. Lastly, we thank the two anonymous reviewers for their constructive feedback that improved this manuscript.

Appendix A. Supplementary data

Supplementary data to this article can be found online at https://doi.org/10.1016/j.margeo.2022.106770.

References

Abessolo, G.O., Almar, R., Jouanno, J., Bonou, F., Castelle, B., Larson, M., 2020. Beach adaptation to intraseasonal sea level changes. Environ. Res. Commun. 2 https://doi.org/10.1088/2515-7620/ab8705, 051003.

Anderson, T.R., Frazer, L.N., Fletcher, C.H., 2010. Transient and persistent shoreline change from a storm. Geophys. Res. Lett. 37 https://doi.org/10.1029/2009GL042252.

Anderson, T.R., Fletcher, C.H., Barbee, M.M., Frazer, L.N., Romine, B.M., 2015. Doubling of coastal erosion under rising sea level by mid-century in Hawaii. Nat. Hazards 78, 75–103. https://doi.org/10.1007/s11069-015-1698-6.

Baldock, T., Ginzo, W., 2020. Morphological response of a reef-fronted beach to sea level rise and reef degradation. Coast. Eng. Proc. 1 https://doi.org/10.9753/icce.v36v.sediment.1.

Baldock, T.E., Golshani, A., Atkinson, A., Shimamoto, T., Wu, S., Callaghan, D.P., Mumby, P.J., 2015. Impact of sea-level rise on cross-shore sediment transport on fetch-limited barrier reef island beaches under modal and cyclonic conditions. Mar. Pollut. Bull. 97, 188–198. https://doi.org/10.1016/j.marpolbul.2015.06.017.

Banno, M., Kuriyama, Y., 2020. Supermoon drives beach morphological changes in the swash zone. Geophys. Res. Lett. 47 https://doi.org/10.1029/2020GL089745.

Barbier, E.B., Hacker, S.D., Kennedy, C., Koch, E.W., Stier, A.C., Silliman, B.R., 2011. The value of estuarine and coastal ecosystem services. Ecol. Monogr. 81, 169–193. https://doi.org/10.1890/10-1510.1.

Barnard, P.L., Short, A.D., Harley, M.D., Splinter, K.D., Vitousek, S., Turner, I.L., Allan, J., Banno, M., Bryan, K.R., Doria, A., Hansen, J.E., Kato, S., Kuriyama, Y., Randall-Goodwin, E., Ruggiero, P., Walker, I.J., Heathfield, D.K., 2015. Coastal vulnerability across the Pacific dominated by El Niño/Southern Oscillation. Nat. Geosci. 8, 801–807. https://doi.org/10.1038/ngeo2539.

Barnard, P.L., Hoover, D., Hubbard, D.M., Snyder, A., Ludka, B.C., Allan, J., Kaminsky, G.M., Ruggiero, P., Gallien, T.W., Gabel, L., McCandless, D., Weiner, H.M., Cohn, N., Anderson, D.L., Serafin, K.A., 2017. Extreme oceanographic forcing and coastal response due to the 2015–2016 El Niño. Nat. Commun. 8, 14365. https://doi.org/10.1038/ncomms14365.

Bochicchio, C., Fletcher, C., Dyer, M., Smith, T., 2009. Reef-top sediment bodies: windward Oʻahu, Hawaiʻi. Pac. Sci. 63, 61–82. https://doi.org/10.2984/1534-6188(2009)63[61:RSBWOH]2.0.CO;2.

Booij, N., Ris, R.C., Holthuijsen, L.H., 1999. A third-generation wave model for coastal regions: 1. Model description and validation. J. Geophys. Res. Oceans 104, 7649–7666. https://doi.org/10.1029/98JC02622.

Bruun, P., 1962. Sea-level rise as a cause of shore erosion. J. Waterw. Harb. Div. 88, 117–130.

Buckley, M.L., Lowe, R.J., Hansen, J.E., van Dongeren, A.R., Storlazzi, C.D., 2018. Mechanisms of wave-driven water level variability on reef-fringed coastlines. J. Geophys. Res. Oceans 123, 3811–3831. https://doi.org/10.1029/2018JC013933.

Burggraaff, O., Schmidt, N., Zamorano, J., Pauly, K., Pascual, S., Tapia, C., Spyrakos, E., Snik, F., 2019. Standardized spectral and radiometric calibration of consumer cameras. Opt. Express 27, 19075–19101. https://doi.org/10.1364/OE.27.019075.

Cai, W., Borlace, S., Lengaigne, M., van Rensch, P., Collins, M., Vecchi, G., Timmermann, A., Santoso, A., McPhaden, M.J., Wu, L., England, M.H., Wang, G., Guilyardi, E., Jin, F.-F., 2014. Increasing frequency of extreme El Niño events due to greenhouse warming. Nat. Clim. Chang. 4, 111–116. https://doi.org/10.1038/nclimate2100.

Cai, W., Wang, G., Santoso, A., McPhaden, M.J., Wu, L., Jin, F.-F., Timmermann, A., Collins, M., Vecchi, G., Lengaigne, M., England, M.H., Dommenget, D., Takahashi, K., Guilyardi, E., 2015. Increased frequency of extreme La Niña events under greenhouse warming. Nat. Clim. Chang. 5, 132–137. https://doi.org/10.1038/nclimate2492.

Caldwell, P.C., Merrifield, M.A., Thompson, P.R., 2015. Sea Level Measured by Tide Gauges from Global Oceans — The Joint Archive for Sea Level holdings (NCEI Accession 0019568). Version 5.5. NOAA National Centers for Environmental Information. https://doi.org/10.7289/V5V40S7W. Dataset.

Casella, E., Rovere, A., Pedroncini, A., Stark, C.P., Casella, M., Ferrari, M., Firpo, M., 2016. Drones as tools for monitoring beach topography changes in the Ligurian Sea (NW Mediterranean). Geo-Mar. Lett. 36, 151–163. https://doi.org/10.1007/s00367-016-0435-9.

Clarke, D., Eliot, I., Frew, J., 1984. Variation in subaerial beach sediment volume on a small sandy beach over a monthly lunar tidal cycle. Mar. Geol. 58.

Conger, C.L., Fletcher, C.H., Barbee, M., 2005. Artificial neural network classification of sand in all visible submarine and subaerial regions of a digital image. J. Coast. Res. 216, 1173–1177. https://doi.org/10.2112/03-0099.1.

Conger, C.L., Fletcher, C.H., Hochberg, E.H., Frazer, N., Rooney, J.J.B., 2009. Remote sensing of sand distribution patterns across an insular shelf: Oahu, Hawaii. Mar. Geol. 267, 175–190. https://doi.org/10.1016/j.margeo.2009.10.005.

Cuttler, M.V.W., Hansen, J.E., Lowe, R.J., Drost, E.J.F., 2018. Response of a fringing reef coastline to the direct impact of a tropical cyclone. Limnol. Oceanogr. Lett. 3, 31–38. https://doi.org/10.1002/lol2.10067.

Dail, H.J., Merrifield, M.A., Bevis, M., 2000. Steep beach morphology changes due to energetic wave forcing. Mar. Geol. 162, 443–458. https://doi.org/10.1016/S0025-3227(99)00072-9.

De Souza, J.M.A.C., Powell, B., 2017. Different approaches to model the nearshore circulation in the south shore of O'ahu, Hawaii. Ocean Sci. 13, 31–46. https://doi.org/10.5194/os-13-31-2017.

Devlin, A.T., Jay, D.A., Talke, S.A., Zaron, E.D., Pan, J., Lin, H., 2017. Coupling of sea level and tidal range changes, with implications for future water levels. Sci. Rep. 7, 17021. https://doi.org/10.1038/s41598-017-17056-z.

El Mrini, A., Anthony, E.J., Maanan, M., Taaouati, M., Nachite, D., 2012. Beach-dune degradation in a Mediterranean context of strong development pressures, and the missing integrated management perspective. Ocean Coast. Manag. 69, 299–306. https://doi.org/10.1016/j.ocecoaman.2012.08.004.

Eltner, A., Kaiser, A., Castillo, C., Rock, G., Neugirg, F., Abellán, A., 2016. Image-based surface reconstruction in geomorphometry – merits, limits and developments. Earth Surf. Dyn. 4, 359–389. https://doi.org/10.5194/esurf-4-359-2016.

Eversole, D., Fletcher, C.H., 2002. Longshore sediment transport rates on a reef-fronted beach: field data and empirical models Kaanapali Beach, Hawaii. J. Coast. Res. 19, 15.

Ferrario, F., Beck, M.W., Storlazzi, C.D., Micheli, F., Shepard, C.C., Airoldi, L., 2014. The effectiveness of coral reefs for coastal hazard risk reduction and adaptation. Nat. Commun. 5, 3794. https://doi.org/10.1038/ncomms4794.

Firing, Y.L., Merrifield, M.A., 2004. Extreme sea level events at Hawaii: influence of mesoscale eddies. Geophys. Res. Lett. 31 https://doi.org/10.1029/2004GL021539.

Fletcher, C.H., Rooney, J.J.B., Barbee, M., Lim, S., Richmond, B., 2003. Mapping shoreline change using digital orthophotogrammetry on Maui, Hawaii. J. Coast. Res. (Special Issue No. 38), 106–124.

Fletcher, C.H., Bochicchio, C., Conger, C.L., Engels, M.S., Feirstein, E.J., Frazer, N., Glenn, C.R., Grigg, R.W., Grossman, E.E., Harney, J.N., Isoun, E., Murray-Wallace, C. V., Rooney, J.J., Rubin, K.H., Sherman, C.E., Vitousek, S., 2008. Geology of Hawaii reefs. In: Riegl, B.M., Dodge, R.E. (Eds.), Coral Reefs of the USA. Springer, Netherlands, Dordrecht, pp. 435–487. https://doi.org/10.1007/978-1-4020-6847-8_11.

Fonstad, M.A., Dietrich, J.T., Courville, B.C., Jensen, J.L., Carbonneau, P.E., 2013. Topographic structure from motion: a new development in photogrammetric measurement. Earth Surf. Process. Landf. 38, 421–430. https://doi.org/10.1002/esp.3366.

Frazer, L.N., Anderson, T.R., Fletcher, C.H., 2009. Modeling storms improves estimates of long-term shoreline change. Geophys. Res. Lett. 36, L20404. https://doi.org/10.1029/2009GL040061.

Gallop, S.L., Bosserelle, C., Pattiaratchi, C.B., Eliot, I., 2011. Hydrodynamic and morphological response of a perched beach during sea breeze activity. J. Coast. Res. 75–79.

Gallop, S.L., Bosserelle, C., Eliot, I., Pattiaratchi, C.B., 2013. The influence of coastal reefs on spatial variability in seasonal sand fluxes. Mar. Geol. 344, 132–143. https://doi.org/10.1016/j.margeo.2013.07.016.

Garza, J.A., Chu, P.-S., Norton, C.W., Schroeder, T.A., 2012. Changes of the prevailing trade winds over the islands of Hawaii and the North Pacific. J. Geophys. Res. Atmos. 117 https://doi.org/10.1029/2011JD016888 n/a-n/a.

Gerritsen, F., 1978. Beach and Surf Parameters in Hawaii. University of Hawaii. Sea Grant College Program.

Gonçalves, J.A., Henriques, R., 2015. UAV photogrammetry for topographic monitoring of coastal areas. ISPRS J. Photogramm. Remote Sens. 104, 101–111. https://doi.org/10.1016/j.isprsjprs.2015.02.009.

Gourlay, M.R., Colleter, G., 2005. Wave-generated flow on coral reefs—an analysis for two-dimensional horizontal reef-tops with steep faces. Coast. Eng. 52, 353–387. https://doi.org/10.1016/j.coastaleng.2004.11.007.

Grady, A.E., Moore, L.J., Storlazzi, C.D., Elias, E, Reidenbach, M.A., 2013. The influence of sea level rise and changes in fringing reef morphology on gradients in alongshore sediment transport. Geophys. Res. Lett. 40 (12), 3096–3101. https://doi.org/10.1002/grl.50577.

Grossman, E.E., Barnhardt, W.A., Hart, P., Richmond, B.M., Field, M.E., 2006. Shelf stratigraphy and the influence of antecedent substrate on Holocene reef development, south Oahu, Hawaii. Mar. Geol. 226, 97–114. https://doi.org/10.1016/j.margeo.2005.09.012.

Habel, S., Fletcher, C.H., Barbee, M., Anderson, T.R., 2016. The influence of seasonal patterns on a beach nourishment project in a complex reef environment. Coast. Eng. 116, 67–76. https://doi.org/10.1016/j.coastaleng.2016.06.006.

Harney, J.N., Fletcher, C.H., 2003. A budget of carbonate framework and sediment production, Kailua Bay, Oahu, Hawaii. J. Sediment. Res. 73, 856–868. https://doi.org/10.1306/051503730856.

Hino, M., Belanger, S.T., Field, C.B., Davies, A.R., Mach, K.J., 2019. High-tide flooding disrupts local economic activity. Sci. Adv. 5 https://doi.org/10.1126/sciadv.aau2736 eaau2736.

Hoegh-Guldberg, O., Mumby, P.J., Hooten, A.J., Steneck, R.S., Greenfield, P., Gomez, E., Harvell, C.D., Sale, P.F., Edwards, A.J., Caldeira, K., Knowlton, N., Eakin, C.M., Iglesias-Prieto, R., Muthiga, N., Bradbury, R.H., Dubi, A., Hatziolos, M.E., 2007. Coral reefs under rapid climate change and ocean acidification. Science 318, 1737–1742. https://doi.org/10.1126/science.1152509.

Homer, P.S., 1964. Characteristics of Deep Water Waves in Oahu Area for a Typical Year. Prepared for the Board of Harbor Commissioners, State of Hawaii. Contract No. 5772. Marine Advisors, La Jolla, California.

Houston, J.R., 2008. The economic value of beaches – A 2008 update. Shore Beach 76, 22–26.

IPCC, 2021. Summary for policymakers. In: Masson-Delmotte, V., Zhai, P., Pirani, A., Connors, S.L., Péan, C., Berger, S., Caud, N., Chen, Y., Goldfarb, L., Gomis, M.I., Huang, M., Leitzell, K., Lonnoy, E., Matthews, J.B.R., Maycock, T.K., Waterfield, T., Yelekçi, O., Yu, R., Zhou, B. (Eds.), Climate Change 2021: The Physical Science Basis. Contribution of Working Group I to the Sixth Assessment Report of the Intergovernmental Panel on Climate Change. Cambridge University Press (In Press).

Isoun, E., Fletcher, C., Frazer, N., Gradie, J., 2003. Multi-spectral mapping of reef bathymetry and coral cover; Kailua Bay, Hawaii. Coral Reefs 22, 68–82. https://doi.org/10.1007/s00338-003-0287-4.

Jeanson, M., Anthony, E.J., Dolique, F., Aubry, A., 2013. Wave characteristics and morphological variations of pocket beaches in a coral reef–lagoon setting, Mayotte Island, Indian Ocean. Geomorphology 182, 190–209. https://doi.org/10.1016/j.geomorph.2012.11.013.

Johnson, N.C., Feldstein, S.B., Tremblay, B., 2008. The continuum of northern hemisphere teleconnection patterns and a description of the NAO shift with the use of self-organizing maps. J. Clim. 21, 6354–6371. https://doi.org/10.1175/2008JCLI2380.1.

Knutson, T., Camargo, S.J., Chan, J.C.L., Emanuel, K., Ho, C.-H., Kossin, J., Mohapatra, M., Satoh, M., Sugi, M., Walsh, K., Wu, L., 2020. Tropical cyclones and climate change assessment: part II: projected response to anthropogenic warming. Bull. Am. Meteorol. Soc. 101, E303–E322. https://doi.org/10.1175/BAMS-D-18-0194.1.

Kohonen, T., 1990. The self-organizing map. Proc. IEEE 78, 1464–1480. https://doi.org/10.1109/5.58325.

Laporte-Fauret, Q., Marieu, V., Castelle, B., Michalet, R., Bujan, S., Rosebery, D., 2019. Low-cost UAV for high-resolution and large-scale coastal dune change monitoring using photogrammetry. J. Mar. Sci. Eng. 7, 63. https://doi.org/10.3390/jmse7030063.

Li, N., Cheung, K.F., Stopa, J.E., Hsiao, F., Chen, Y.-L., Vega, L., Cross, P., 2016. Thirty-four years of Hawaii wave hindcast from downscaling of climate forecast system reanalysis. Ocean Model 100, 78–95. https://doi.org/10.1016/j.ocemod.2016.02.001.

Liu, Y., Weisberg, R.H., Mooers, C.N.K., 2006. Performance evaluation of the self-organizing map for feature extraction. J. Geophys. Res. 111, C05018. https://doi.org/10.1029/2005JC003117.

Long, X., Widlansky, M.J., Schloesser, F., Thompson, P.R., Annamalai, H., Merrifield, M. A., Yoon, H., 2020. Higher sea levels at Hawaii caused by strong El Niño and weak trade winds. J. Clim. 33, 3037–3059. https://doi.org/10.1175/JCLI-D-19-0221.1.

Miller, T., Fletcher, C., 2003. Waikiki: historical analysis of an engineered shoreline. J. Coast. Res. 19, 1026–1043.

Monismith, S.G., Herdman, L.M.M., Ahmerkamp, S., Hench, J.L., 2013. Wave transformation and wave-driven flow across a steep coral reef. J. Phys. Oceanogr. 43, 1356–1379. https://doi.org/10.1175/JPO-D-12-0164.1.

NOAA, 2020. National Oceanic and Atmospheric Administration (2020). Tides & Currents. Tide Station 1612340 Station Info [WWW Document]. http://tidesandcurrents.noaa.gov/inventory.html?id1/41612340 accessed 7.20.20.

Nolet, C., van Puijenbroek, M., Suomalainen, J., Limpens, J., Riksen, M., 2018. UAV-imaging to model growth response of marram grass to sand burial: implications for coastal dune development. Aeolian Res. 31, 50–61. https://doi.org/10.1016/j.aeolia.2017.08.006.

Norcross, Z.M., Fletcher, C.H., Merrifield, M., 2002. Annual and interannual changes on a reef-fringed pocket beach: Kailua Bay, Hawaii. Mar. Geol. 190, 553–580. https://doi.org/10.1016/S0025-3227(02)00481-4.

Norcross, Z., Fletcher, C., Rooney, J., Eversole, D., Miller, T., 2003. Hawaiian Beaches Dominated by Longshore Transport.

Oppenheimer, M., Glavovic, B.C., Hinkel, J., van de Wal, R., Magnan, A.K., Abd-Elgawad, A., Cai, R., Cifuentes-Jara, M., Rica, C., DeConto, R.M., Ghosh, T., Hay, J., Islands, C., Isla, F., Marzeion, B., Meyssignac, B., Sebesvari, Z., Biesbroek, R., Buchanan, M.K., de Campos, R.S., Cozannet, G.L., Domingues, C., Dangendorf, S., Döll, P., Duvat, V.K.E., Edwards, T., Ekaykin, A., Frederikse, T., Gattuso, J.-P., Kopp, R., Lambert, E., Lawrence, J., Narayan, S., Nicholls, R.J., Renaud, F., Simm, J., Smit, A., Woodruff, J., Wong, P.P., Xian, S., Abe-Ouchi, A., Gupta, K., Pereira, J., 2019. Sea Level Rise and Implications for Low-Lying Islands, Coasts and Communities (IPCC Special Report on the Ocean and Cryosphere in a Changing Climate).

Özkan-Haller, H.T., Vidal, C., Losada, I.J., Medina, R., Losada, M.A., 2001. Standing edge waves on a pocket beach. J. Geophys. Res. Oceans 106, 16981–16996. https://doi.org/10.1029/1999JC000193.

PacIOOS, 2021a. Simulating WAves Nearshore (SWAN) Regional Wave Model: Oahu. Metadata [WWW Document]. https://www.pacioos.hawaii.edu/metadata/swan_oahu.html (accessed 2.1.21).

PacIOOS, 2021b. Pacific Islands Ocean Observing System (PacIOOS). Wave Run-Up Forecast: Waikīkī, O'ahu (about) [WWW Document]. https://www.pacioos.hawaii.edu/shoreline/runup-waikiki/#about (accessed 2.1.21).

Pagán, J.I., Bañón, L., López, I., Bañón, C., Aragonés, L., 2019. Monitoring the dune-beach system of Guardamar del Segura (Spain) using UAV, SfM and GIS techniques. Sci. Total Environ. 687, 1034–1045. https://doi.org/10.1016/j.scitotenv.2019.06.186.

Pandolfi, J.M., Connolly, S.R., Marshall, D.J., Cohen, A.L., 2011. Projecting coral reef futures under global warming and ocean acidification. Science 333, 418–422. https://doi.org/10.1126/science.1204794.

Parsons, L.A., Coats, S., 2019. Ocean-atmosphere trajectories of extended drought in Southwestern North America. J. Geophys. Res. Atmos. 124, 8953–8971. https://doi.org/10.1029/2019JD030424.

Parsons, L.A., Coats, S., Overpeck, J.T., 2018. The continuum of drought in Southwestern North America. J. Clim. 31, 8627–8643. https://doi.org/10.1175/JCLI-D-18-0010.1.
Péquignet, A.-C., Becker, J.M., Merrifield, M.A., Boc, S.J., 2011. The dissipation of wind wave energy across a fringing reef at Ipan, Guam. Coral Reefs 30, 71–82. https://doi.org/10.1007/s00338-011-0719-5.
Pomeroy, A., Lowe, R., Symonds, G., Van Dongeren, A., Moore, C., 2012. The dynamics of infragravity wave transformation over a fringing reef. J. Geophys. Res. Oceans 117. https://doi.org/10.1029/2012JC008310.
Potemra, J.T., Lukas, R., 1999. Seasonal to interannual modes of sea level variability in the western Pacific and eastern Indian oceans. Geophys. Res. Lett. 26, 365–368. https://doi.org/10.1029/1998GL900280.
Reusch, D.B., Alley, R.B., Hewitson, B.C., 2005. Relative performance of self-organizing maps and principal component analysis in pattern extraction from synthetic climatological data. Polar Geogr. 29, 188–212. https://doi.org/10.1080/789610199.
Risandi, J., Hansen, J.E., Lowe, R.J., Rijnsdorp, D.P., 2020. Shoreline variability at a reef-fringed pocket beach. Front. Mar. Sci. 7 https://doi.org/10.3389/fmars.2020.00445.
Roman-Rivera, M., Ellis, J., 2018. The king tide conundrum. J. Coast. Res. 344, 769–771. https://doi.org/10.2112/JCOASTRES-D-18A-00001.1.
Romine, B.M., Fletcher, C.H., Barbee, M.M., Anderson, T.R., Frazer, L.N., 2013. Are beach erosion rates and sea-level rise related in Hawaii? Glob. Planet. Chang. 108, 149–157. https://doi.org/10.1016/j.gloplacha.2013.06.009.
Scarelli, F.M., Sistilli, F., Fabbri, S., Cantelli, L., Barboza, E.G., Gabbianelli, G., 2017. Seasonal dune and beach monitoring using photogrammetry from UAV surveys to apply in the ICZM on the Ravenna coast (Emilia-Romagna, Italy). Remote Sens. Appl. Soc. Environ. 7, 27–39. https://doi.org/10.1016/j.rsase.2017.06.003.
Segura, L.E., Hansen, J.E., Lowe, R.J., 2018. Seasonal shoreline variability induced by subtidal water level fluctuations at reef-fringed beaches. J. Geophys. Res. Earth Surf. 123, 433–447. https://doi.org/10.1002/2017JF004385.
Siegle, E., Costa, M.B., 2017. Nearshore wave power increase on reef-shaped coasts due to sea-level rise. Earths Future 5, 1054–1065. https://doi.org/10.1002/2017EF000624.
Stevenson, S., Wittenberg, A.T., Fasullo, J., Coats, S., Otto-Bliesner, B., 2021. Understanding diverse model projections of future extreme El Niño. J. Clim. 34, 449–464. https://doi.org/10.1175/JCLI-D-19-0969.1.
Tarui, N., Peng, M., Eversole, D., 2018. Economic Impact Analysis of the Potential Erosion of Waikīkī Beach. A 2016 Update. University of Hawai'i Sea Grant College Program.
Theuerkauf, E.J., Rodriguez, A.B., Fegley, S.R., Luettich, R.A., 2014. Sea level anomalies exacerbate beach erosion. Geophys. Res. Lett. 41, 5139–5147. https://doi.org/10.1002/2014GL060544.
Thompson, P.R., Widlansky, M.J., Merrifield, M.A., Becker, J.M., Marra, J.J., 2019. A statistical model for frequency of coastal flooding in Honolulu, Hawaii, during the 21st century. J. Geophys. Res. Oceans 124, 2787–2802. https://doi.org/10.1029/2018JC014741.
Thompson, P.R., Widlansky, M.J., Hamlington, B.D., Merrifield, M.A., Marra, J.J., Mitchum, G.T., Sweet, W., 2021. Rapid increases and extreme months in projections of United States high-tide flooding. Nat. Clim. Chang. 11, 584–590. https://doi.org/10.1038/s41558-021-01077-8.
Turner, I.L., Harley, M.D., Drummond, C.D., 2016. UAVs for coastal surveying. Coast. Eng. 114, 19–24. https://doi.org/10.1016/j.coastaleng.2016.03.011.
USGS, 2017a. Agisoft Photoscan Workflow. United States Geological Survey [WWW Document] (accessed 2.1.19). https://uas.usgs.gov/nupo/pdf/USGSAgisoftPhotoScanWorkflow.pdf.
USGS, 2017b. Unmanned Aircraft Systems Post Processing; Structure-from-motion photogrammetry. United States Geological Survey. March 2017 [WWW Document] (accessed 2.1.19). https://uas.usgs.gov/nupo/pdf/PhotoScanProcessingDSLRMar2017.pdf.
Varela, M.R., Patrício, A.R., Anderson, K., Broderick, A.C., DeBell, L., Hawkes, L.A., Tilley, D., Snape, R.T.E., Westoby, M.J., Godley, B.J., 2019. Assessing climate change associated sea-level rise impacts on sea turtle nesting beaches using drones, photogrammetry and a novel GPS system. Glob. Chang. Biol. 25, 753–762. https://doi.org/10.1111/gcb.14526.
Vitousek, S., Fletcher, C.H., 2008. Maximum annually recurring wave heights in Hawai'i. Pac. Sci. 62, 541–553. https://doi.org/10.2984/1534-6188(2008)62[541:MARWHI]2.0.CO;2.
Vos, K., Harley, M., Turner, I., Splinter, K., 2021. Large Regional Variability in Coastal Erosion Caused by ENSO (Preprint). In Review. https://doi.org/10.21203/rs.3.rs-666160/v1.
Widlansky, M.J., Long, X., Schloesser, F., 2020. Increase in sea level variability with ocean warming associated with the nonlinear thermal expansion of seawater. Commun. Earth Environ. 1, 1–12. https://doi.org/10.1038/s43247-020-0008-8.
Wiegel, R.L., 2008. Waikiki Beach, Oahu, Hawaii: history of its transformation from a natural to an urban shore. Shore Beach 76, 28.
Winter, G., Lowe, R.J., Symonds, G., Hansen, J.E., van Dongeren, A.R., 2017. Standing infragravity waves over an alongshore irregular rocky bathymetry. J. Geophys. Res. Oceans 122, 4868–4885. https://doi.org/10.1002/2016JC012242.
Wright, L.D., Short, A.D., 1984. Morphodynamic variability of surf zones and beaches: a synthesis. Mar. Geol. 56, 93–118.